# Investigation and Experimental Test of Fault-Tolerant Operation of a Mutually Coupled Dual Three-Phase SRM Drive Under Faulty Conditions

Wen Ding, *Member, IEEE*, Yanfang Hu, and Luming Wu

***Abstract*—The mutually coupled dual three-phase switched reluctance motor (DTPSRM) is a new type of special 12/8 SRMs, which possesses high-reliability and fault-tolerant feature. In the past researches, the model, analysis, and fault-tolerant operation were mainly focused on the classical single three- and four-phase SRMs. This paper is mainly to analyze and investigate the fault-tolerant performances of a 12/8-pole mutually coupled DTPSRM drive under various open-circuit operations. First, the static magnetic characteristics of DTPSRM with single- and two-phase excitations are calculated by finite-element analysis. Then, the mathematic model of the DTPSRM drive under open-circuit condition is developed with a combination of state and fault functions. The simulation model of the DTPSRM drive system with a fault-tolerant control strategy is established for dynamic analysis. The faulty characteristics and fault-tolerant performances of the DTPSRM with diverse open circuits are predicted. Finally, a 12/8 DTPSRM is prototyped and an experimental setup is built for verification. The experimental normal results and diverse open-circuit operations and self-starting capability under lack of phases are presented, validating the accuracy of the analysis and simulation as well as fault-tolerant characteristics of the DTPSRM drive system.**

***Index Terms*—Dual three-phase switched reluctance motor (DTPSRM), fault tolerant, mutually coupled, open circuit, simulation model.**

## I. INTRODUCTION

THE fault tolerance of motor drives has been attracting more and more interests during the last several years. In some safety-critical applications like more electric aircraft (MEA), electromechanical and electrohydraulic actuators, aerospace, military fields, electric and hybrid electric vehicles (EV/HEV), it is crucial for the motor drive to continue operation under diverse fault conditions. Many literatures have been presented to investigate on the modeling, analysis, and testing of fault-tolerant rotor permanent-magnet (PM) brushless [1]–[4] and induction motor drives. Stator PM motor drives are gaining an increasing attention in the HEV application owing to their advantages such as high power/torque density and high efficiency. In [5], Zhao analyzes the fault-tolerant characteristic of a doubly salient PM (DSPM) motor drive by using a cosimulation model with considering the direct field-circuit coupling. A remedial brushless ac remedial strategy for the DSPM motor drive under fault-tolerant operation has been proposed and implemented in [6]. Furthermore, another type of stator PM motor which is termed as flux-switching PM motor and its control strategies with different degrees of fault-tolerant capability have been investigated in [7] and [8]. However, the stator PM motors have also some disadvantages such as poor mechanical structure and difficulty in PM cooling because the PMs are located in the stator. Recently, the multiphase induction motors have also been gaining more and more interests for fault-tolerant and high-power applications. In [9] and [10], the modeling and control of a six-phase symmetrical induction machine drive under open-circuit operation have been presented.

In order to improve the fault tolerance and enhance the reliability of motor drives in the electrical system, the concept of dual three-phase motor drives is widely proposed for MEA, EV/HEV, wind power generation, ship propulsion, rail traction, and high-power industrial applications. A dual three-phase induction motor fed by two sets of voltage source inverters and its control strategies such as direct torque control and predictive control was investigated in [11]–[13]. Furthermore, the impact of winding arrangement and a set of experimental tests on a dual three-phase induction motor for fault-tolerant applications have been described in [14] and [15]. Additionally, there are also some literatures which have reported the multiphase PM motor drives for fault-tolerant applications in recent years. In [16], a 12-slot 10-pole PM motor, which is designed with dual three-phase winding, has been analyzed and investigated in healthy and faulty operating conditions. The effects of the different coil configurations have also been investigated. In [17], a control algorithm for driving two three-phase PM motors with the reduced-component-count dual integrated inverter was presented and tested. In [18], an improved vector space decomposition current control scheme for dual three-phase PM synchronous motors accounting for the current unbalance and the fifth, seventh current harmonics is proposed. In [19], the sensorless rotor position detention capability of a dual three-phase PM motor drive under healthy and faulty operating conditions is investigated.

Switched reluctance motors (SRMs) have simple structure, low cost and manufacturing complexity due to the absence of

---

Manuscript received June 29, 2014; revised November 1, 2014 and September 18, 2014; accepted December 22, 2014. Date of publication January 12, 2015; date of current version August 21, 2015. This work was supported by the National Natural Science Foundation of China under Grant 51477130 and Grant 51007071, Natural Science Basic Research Plan in Shaanxi Province under Grant 2014JM7247, and the State Key Laboratory of Electrical Insulation and Power Equipment under Grant EIPE14315. Recommended for publication by Associate Editor J. Hur.

The authors are with the State Key Laboratory of Electrical Insulation and Power Equipment, School of Electrical Engineering, Xi'an Jiaotong University, Xi'an 710049, China (e-mail: wending@mail.xjtu.edu.cn; stiwen@163.com; 3137203346@qq.com).

Color versions of one or more of the figures in this paper are available online at http://ieeexplore.ieee.org.

Digital Object Identifier 10.1109/TPEL.2015.2389258

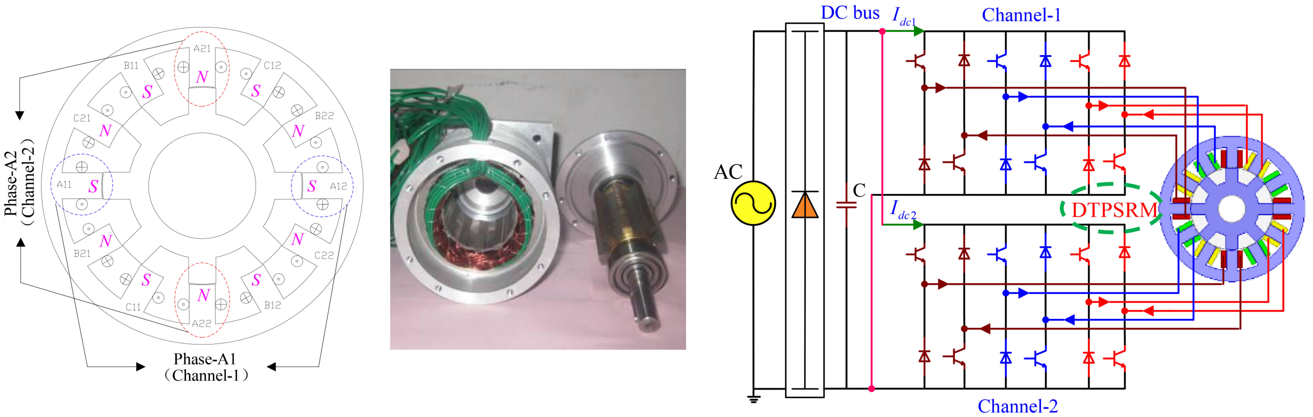

(a) (b) (c)

Fig. 1. (a) and (b) Schematic and prototype of the mutually coupled DTPSRM. (c) Drive topology of the DTPSRM.

windings and PMs on the rotor, which is gaining great attention in high-reliability and high-speed applications. In the past years, many studies have analyzed and investigated the fault-tolerant operations, characteristics, and detection and diagnosis methods for classical SRM drives. For example, the classification of electrical faults in SRM drives, several fault detection devices, artificial-neural-network fault-tolerant model and finite-element analysis (FEA), several remedial strategies for short and open circuits, and new comprehensive detection methods of eccentricity fault using high-frequency injection signal, and real-time diagnosis of power converter faults in SRM drives have been reported in [20]–[26], respectively. However, in most of above literatures, the modeling, analysis, and control strategy of fault-tolerant operation were discussed only for the classical single three-phase 6/4 and 8/6 SRMs.

The dual three-phase SRM (DTPSRM) is a new kind of special SRMs, which is employed the redundant technology in the classical 12/8 SRM, for high-reliability and fault-tolerant operations in some critical applications. The 12-pole windings of the classical 12/8 SRM are divided in two symmetrical three-phase winding units and each winding unit is connected to an independent set of asymmetric half-bridge power converter. It is confirmed that this type of DTPSRMs would be very suitable for developing future integrated high-power and high-torque fault-tolerant motor/generator with redundancy to enhance reliability in some safety-critical applications such as MEA and EV/HEV. In [27], a nonlinear equivalent magnetic circuit modeling method is developed to calculate the static phase flux linkages of a low-speed DTPSRM by using the formulas of the air-gap and other iron-core permeances. In [28], a 12/8-pole DTPSRM prototype with the power of 250 kW and its experimental drive system are presented for aircraft engine starter/generator application. The FEA static flux linkage and torque characteristics and experimental dynamic results at normal conditions are presented. In [29], the authors proposed a dynamic modeling that accounts for the effect of mutual coupling between two channels but without consideration of magnetic saturation for the DTPSRM operation under dual-channel mode (DCM). After that, the simulation model and steady-state and transient performances for the low-speed DTPSRM applied as a generator operation under SCM and DCM were also presented and compared in [30], respectively. Furthermore, an improved decoupled model of the mutually coupled DTPSRM operation under DCM is also proposed in [31], which is based on the equivalent inductance and flux-linkage characteristics that consider magnetic saturation. Moreover, a comparative study of magnetic characteristics and dynamic performances for two mutually coupled DTPSRMs with the same properties and different winding connections is presented in [32]. Unfortunately, most of the above analysis, modeling and simulation for the DTPSRM drive were only based on the normal conditions rather than on the fault-tolerant operation and control.

This paper is mainly to analyze and investigate the fault-tolerant characteristic and behavior of mutually coupled DTPSRM drives under various open-circuit operating conditions. In Section II, the 12/8-pole mutually coupled DTPSRM prototype and the magnetic characteristics of the DTPSRM are presented. The mathematic model under open-circuit faulty condition is derived and developed in Section III. The whole simulation model with fault-tolerant closed-loop control is established to predict the steady-state and transient behaviors of the DTPSRM drive under open-circuit faults in Section IV. The experimental drive platform of the prototype DTPSRM is built in Section V. The experimental results at normal and various open-circuit faulty operations and self-starting capability under lack of one and two phases are presented to verify the analytical and simulation results and fault-tolerant control. Finally, conclusions are drawn in Section VI.

## II. MACHINE TOPOLOGY AND FEA

### A. *Configuration of the DTPSRM Drive System*

The schematic prototype of a mutually coupled DTPSRM and its drive topology with two asymmetric half-bridge converters are shown in Fig. 1. The 12 stator pole coils are divided into dual three-phase winding units in a dual-channel topology and the two coils on opposite poles are in series connection to make up one phase in one channel. The magnetic polarity

TABLE I
MAIN DIMENSIONS OF THE DTPSRM PROTOTYPE

| Number of stator poles | 12 | Number of rotor poles | 8 |
|---|---|---|---|
| Outer diameter of stator | 80 mm | Stator yoke width | 6 mm |
| Outer diameter of rotor | 45 mm | Rotor yoke width | 6 mm |
| Stack length | 45.8 mm | Arc angle of stator pole | 15° |
| Airgap length | 0.25 mm | Arc angle of rotor pole | 17° |

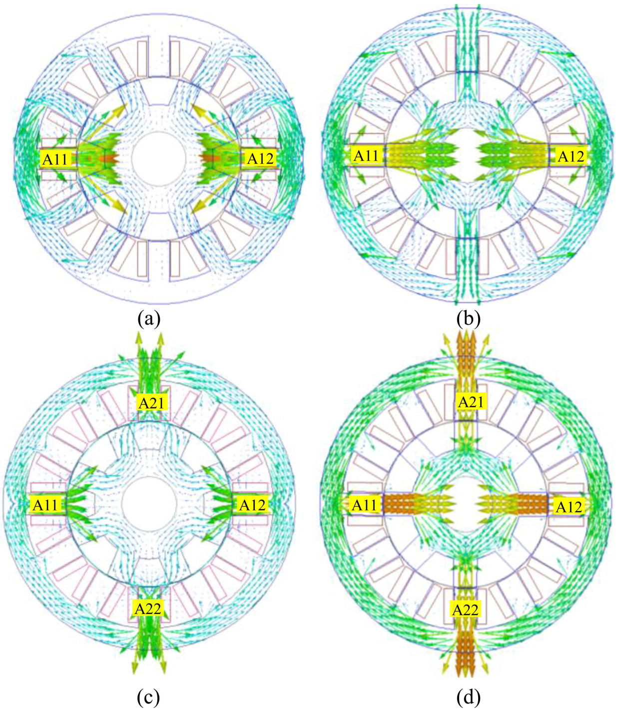

Fig. 2. Magnetic flux lines of the DTPSRM with (a) and (b) SPE (A1) at the unaligned and aligned positions, (c) and (d) TPE (A1 and A2) at the unaligned and aligned positions.

"NSNSNSNSNSNS" is formed on the stator poles owing to the given winding configuration, as shown in Fig. 1(a). The six-phase windings of the DTPSRM are supplied by two power electronic converters, which consist of two independent sets of asymmetric half bridges with two controllers to achieve high fault tolerance, as shown in Fig. 1(c). The dc-link voltage is established by a diode rectifier from ac variable transformer and is controlled by the variable ac power supply. Once a power converter or controller fails, the drive system becomes a single three-phase SRM drive for continuous operation. Table I gives the key parameters of the DTPSRM prototype.

## B. Static Magnetic Characteristics

Generally, FEA is a suitable method for machine design and performance prediction. In this paper, the FEA software Ansoft/Maxwell 16.0 is used to analyze the magnetic field distribution and calculate the inductance, flux linkage, and torque characteristics. Fig. 2 shows the magnetic field distributions of the DTPSRM at the unaligned ($\theta = 0°$) and aligned ($\theta = 22.5°$) positions with single-phase excitation (SPE) and two-phase excitation (TPE) modes. It can be seen from Fig. 2(a) and (b) that there is a short flux path pattern under SPE. In this situation, there are mutual coupling fluxes in the neighboring phases, but the directions of the mutual flux in all neighboring phases are different. It can be seen from Fig. 2(c) and (d) that there is also a short flux path pattern and the DTPSRM has two pairs of magnetic polarities under simultaneous TPE. In this situation, there are only mutual coupling fluxes, which are always positive in conducting phases A1 and A2 due to the winding connection of magnetic polarity "NSNSNSNSNSNS," while there are no mutual coupling fluxes in other neighboring phases. The magnetic field is also symmetrical.

Fig. 3 shows the self- and mutual flux-linkage characteristics of this DTPSRM with SPE ($x1$) ($x$ represent A, B, C). However, in most situations, the currents of phases $x1$ and $x2$ in the two channels are almost the same ($i_{x1} = i_{x2}$) and synchronized under DCM due to the symmetrical structure of the motor. At this operation, the magnetic material in some regions of the DTPSRM will be saturated if the phase currents are large and the flux linkage of each phase will be somewhat reduced because of such saturation. Fig. 4 shows the equivalent self-, total, and mutual flux-linkage characteristics in one phase when two phases ($x1$ and $x2$) are simultaneously excited and the magnetic saturation is also considered. In these figures, the flux linkages are obtained from the FEA simulations and phases $x1$ and $x2$ are both excited with the same current levels at different rotor positions, and Table II gives the comparison of diverse phase flux linkages with different excitation modes at different positions. It can be found from Figs. 3 and 4 that the phase flux linkage around the aligned position becomes to be saturated as the phase current is larger than 20 A under SPE, while the phase flux linkage at the same region will begin to be saturated as the phase currents are larger than 13 A under simultaneous TPE ($x1$ and $x2$). It can also be found that the phase self- and mutual flux linkages are almost the same in the linear magnetic region under two excitation modes, respectively, while the phase self- and mutual flux linkages in the magnetic saturation region under TPE are lower than those under SPE. For example, $\lambda_{x1,\text{self}}$ at $i_{x1} = i_{x2} = 5$ A and $i_{x1} = i_{x2} = 25$ A under TPE at the aligned position are 5.546 and 19.35 mWb, which are 99.9% and 77.1% of $\lambda_{x1,\text{self}}$ at $i_{x1} = 5$ A and $i_{x1} = 25$ A under SPE.

The static torque characteristics of this DTPSRM with SPE and TPE are also calculated, as shown in Fig. 5. Furthermore, the maximum and average torques at different current levels during one half of excitation cycle are given in Table III. It can be found that the average and maximum torques developed with TPE are larger than two times of those with SPE at the same currents.

In summary, this DTPSRM can be called as a new type of mutually coupled DTPSRM because the dual three-phase winding units in the motor would have strong magnetically coupling when they are excited simultaneously and operating under DCM.

# III. MODELING OF DTPSRM WITH OPEN-CIRCUIT OPERATION

From above analysis and calculation, the DTPSRM looks like a DTPSRM under the normal DCM operation. The voltage drops of freewheeling diode and switch conduction are normally

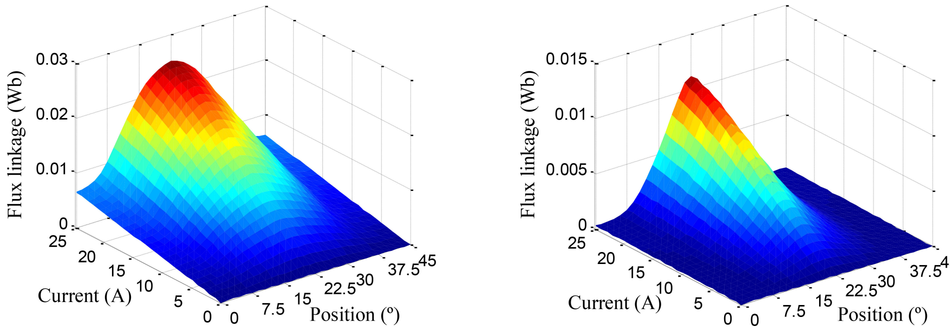

(a) (b)

Fig. 3. Static flux-linkage characteristics when only one phase ($x1$) is excited. (a) Self-flux linkage in phase $x1$. (b) Mutual flux linkage in phase $x2$.

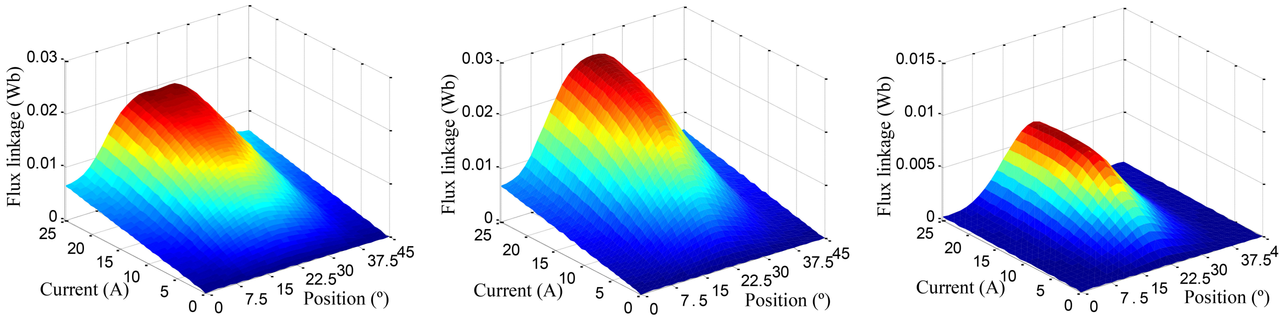

(a) (b) (c)

Fig. 4. Flux-linkage characteristics of the mutually coupled DTPSRM under TPE. (a) Equivalent self-flux linkage in phase $x1$. (b) Total flux linkage in one phase. (c) Mutual flux linkage between phases $x1$ $x2$.

TABLE II
COMPARISON OF STATIC FLUX LINKAGE FOR DIFFERENT CURRENT LEVELS

| Current | 5 A | 10 A | 15 A | 20 A | 25 A |
|---|---|---|---|---|---|
| Phase self-flux linkage with SPE at 0°, mWb | 1.285 | 2.572 | 3.856 | 5.025 | 6.442 |
| Phase equivalent self-flux linkage with TPE at 0°, mWb | 1.285 | 2.570 | 3.855 | 5.141 | 6.427 |
| Phase total flux linkage with TPE at 0°, mWb | 1.340 | 2.681 | 4.021 | 5.362 | 6.703 |
| Phase self-flux linkage with SPE at 22.5°, mWb | 5.551 | 11.12 | 16.68 | 21.45 | 25.09 |
| Phase equivalent self-flux linkage with TPE at 22.5°, mWb | 5.546 | 11.10 | 15.38 | 17.80 | 19.35 |
| Phase total flux linkage under TPE at 22.5°, mWb | 8.011 | 16.05 | 22.13 | 24.78 | 26.13 |

ignored and the full dc-bus voltage is applied across the conducting phase windings in two channels, then the single-phase voltage and flux-linkage equations of the DTPSRM under normal operation can be described by

$$\begin{cases} V_{\mathrm{dc}} - \xi_j u_j = 0, (j = A1, B1, C1, A2, B2, C2) \\ \varphi_j = \varphi(\theta_j, i_{A1}, i_{B1}, i_{C1}, i_{A2}, i_{B2}, i_{C2}) \end{cases} \tag{1}$$

where $V_{\mathrm{dc}}$ is the dc-bus voltage, $u_j$ is the $j$th-phase terminal voltage, $\varphi_j$ is the phase flux linkage, and $\xi_j$ is a state function, which is used to represent the state of the $j$th-phase winding. It can be expressed as

$$\xi_j = \begin{cases} 1, & \theta_{\mathrm{on}} \leq \theta \leq \theta_{\mathrm{off}} \\ -1, & \theta \geq \theta_{\mathrm{off}} \end{cases} \tag{2}$$

where 1 and –1 denote energized and freewheeling states, respectively.

To derive the mathematical model of the DTPSRM drive under fault condition, the phase A1 is assumed to be an open circuit at some point. If the phase A1 is excited at this time, then the voltage across the phase A1 is zero. If the phase is during freewheeling state, then the voltage and current of phase A1 remain unaffected. An open-circuit fault function is introduced as follows: where

$$\chi_{A1} = \begin{cases} 0, & \mathrm{phase\ A1\ open-circuited\ and\ } \xi_{A1} = 1 \\ 1, & \xi_{A1} = -1 \end{cases}. \tag{3}$$

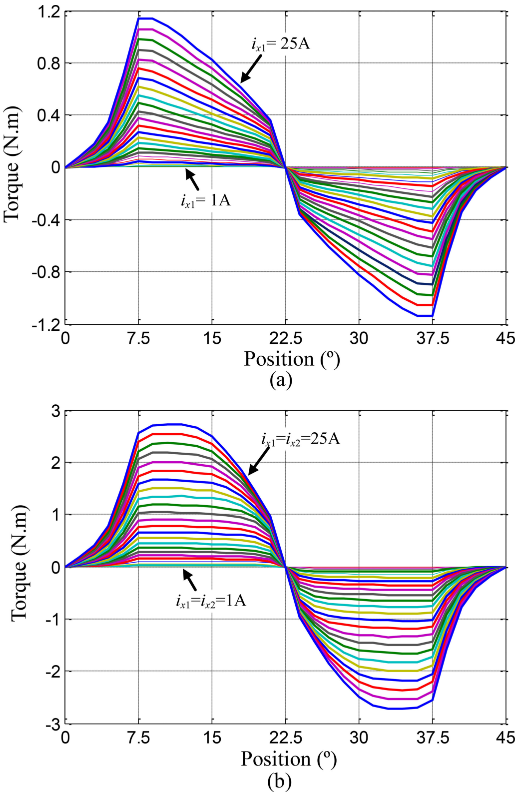

Fig. 5. Static torque characteristics of the DTPSRM with different excitations: (a) SPE (*x*1) and (b) TPE (*x*1 and *x*2).

Therefore, the first equation in the mathematical model (1) with one-phase (A1) open-circuit fault is expressed as

$$\begin{cases} \chi_{A1}V_{\mathrm{dc}}-\xi_{A1}u_{A1}=0, \quad V_{\mathrm{dc}}-\xi_{B1}u_{B1}=0, \quad V_{\mathrm{dc}}-\xi_{C1}u_{C1}=0 \\ V_{\mathrm{dc}}-\xi_{A2}u_{A2}=0, \quad V_{\mathrm{dc}}-\xi_{B2}u_{B2}=0, \quad V_{\mathrm{dc}}-\xi_{C2}u_{C2}=0 \end{cases} \tag{4}$$

From above description in Section II-B, it is concluded that the DTPSRM could be considered as a DTPSRM when it is operating under DCM. In this operation, there are only positive mutual coupling fluxes in conducting phases A1 and A2 due to the winding connection of magnetic polarity "NSNSNSNSNSNS," and no mutual coupling fluxes in other neighboring phases.

TABLE III

COMPARISON OF STATIC TORQUE FOR DIFFERENT CURRENT LEVELS, UNIT:N·M

| Current | 5 A | 10 A | 15 A | 20 A | 25 A |
|---|---|---|---|---|---|
| Average torque with SPE | 0.026 | 0.102 | 0.230 | 0.407 | 0.620 |
| Average torque with TPE | 0.079 | 0.320 | 0.707 | 1.158 | 1.621 |
| Maximum torque with SPE | 0.051 | 0.205 | 0.459 | 0.790 | 1.179 |
| Maximum torque with TPE | 0.124 | 0.498 | 1.115 | 1.916 | 2.809 |

Thus, the dual-phase (A1 and A2) voltage equations under DCM can be described as follows [31]: (6) shown at the bottom of the page

$$u_{A1}=\frac{d\varphi_{A1}}{dt}+r\cdot i_{A1},\ \text{and}\ u_{A2}=\frac{d\varphi_{A2}}{dt}+r\cdot i_{A2} \tag{5}$$

where A1 and A2 are the simultaneous conducting phases in channel 1 and 2, respectively. $\varphi_{A1}$ and $\varphi_{A2}$ are the total flux linkages in phases A1 and A2, respectively. $\varphi_{A1A1}$ and $\varphi_{A2A1}$ are the equivalent self-flux linkage and mutual flux linkage in phase A1. The meaning of $\varphi_{A1A2}$ is similar to $\varphi_{A2A1}$.

Furthermore, owing to the symmetrical construction of the DTPSRM, the currents of phases A1 and A2 are always equal to each other at any time under DCM operation. The self- and mutual flux linkages in phases A1 and A2 will also keep the same. Thus, it can be assumed that $i_{A1}=i_{A2}=i$, $\varphi_{A1A1}=\varphi_{A2A2}$, and $\varphi_{A1A2}=\varphi_{A2A1}$ under DCM operation.

In addition, the total torque developed by phases A1 and A2 under DCM operation is expressed as

$$\begin{aligned} T_{A1A2}(\theta,i_{A1},i_{A2}) &= T_{A1A2}(\theta,i_{A1}=i,i_{A2}=i) \\ &= T_{eq}(\theta,i_{A1}=i_{A2}=i). \end{aligned} \tag{7}$$

As discussed before, there are only mutual coupling fluxes in conducting phases A1 and A2 and no mutual coupling fluxes in other neighboring phases, then the above mathematic equation (see 4) with one-phase (A1) open-circuit fault becomes as follows: (8) shown at the bottom of the page. (9) Shown on the next page.

Equation (8) is a complicated nonlinear, time-varying, and unsteady partial differential equation. We can apply the Cramer's rule to get the following: (10) shown on bottom of the next page.

$$\left.\begin{aligned} \varphi_{A1}=\varphi_{A1}(i_{A1},i_{A2},\theta) &= \underbrace{\varphi_{A1A1}(i_{A1},i_{A2},\theta)}_{\substack{\text{self flux linkage of phase A1}\\ \text{undertwo-phase excitation}}}+\underbrace{\varphi_{A2A1}(i_{A2},i_{A1},\theta)}_{\substack{\text{mutual flux linkage in phase A1}\\ \text{under two-phase excitation}}} \\ \varphi_{A2}=\varphi_{A2}(i_{A2},i_{A1},\theta) &= \underbrace{\varphi_{A2A2}(i_{A2},i_{A1},\theta)}_{\substack{\text{self flux linkage of phase A2}\\ \text{under two-phase excitation}}}+\underbrace{\varphi_{A1A2}(i_{A1},i_{A2},\theta)}_{\substack{\text{mutual flux linkage in phase A2}\\ \text{under two-phase excitation}}} \end{aligned}\right\} \tag{6}$$

$$\begin{cases} \xi_{A1}\left(\frac{\partial\varphi_{A1}}{\partial i_{A1}}\frac{di_{A1}}{dt}+\frac{\partial\varphi_{A1}}{\partial i_{A2}}\frac{di_{A2}}{dt}\right)=P_{A1},\xi_{A2}\left(\frac{\partial\varphi_{A2}}{\partial i_{A1}}\frac{di_{A1}}{dt}+\frac{\partial\varphi_{A2}}{\partial i_{A2}}\frac{di_{A2}}{dt}\right)=P_{A2} \\ \xi_{B1}\left(\frac{\partial\varphi_{B1}}{\partial i_{B1}}\frac{di_{B1}}{dt}+\frac{\partial\varphi_{B1}}{\partial i_{B2}}\frac{di_{B2}}{dt}\right)=P_{B1},\xi_{B2}\left(\frac{\partial\varphi_{B2}}{\partial i_{B1}}\frac{di_{B1}}{dt}+\frac{\partial\varphi_{B2}}{\partial i_{B2}}\frac{di_{B2}}{dt}\right)=P_{B2} \\ \xi_{C1}\left(\frac{\partial\varphi_{C1}}{\partial i_{C1}}\frac{di_{C1}}{dt}+\frac{\partial\varphi_{C1}}{\partial i_{C2}}\frac{di_{C2}}{dt}\right)=P_{C1},\xi_{C2}\left(\frac{\partial\varphi_{C2}}{\partial i_{C1}}\frac{di_{C1}}{dt}+\frac{\partial\varphi_{C2}}{\partial i_{C2}}\frac{di_{C2}}{dt}\right)=P_{C2} \end{cases} \tag{8}$$

where $F_{A1}(i_{A1}, i_{A2}, V_{\mathrm{dc}}, \theta, \xi_{A1}, \xi_{A2})$ is expressed as (11) shown at the bottom of the next page. $F_{B1}, F_{C1}, F_{A2}, F_{B2}$ and $F_{C2}$ are similar to $F_{A1}$.

Here, we introduced two variables as (12) to simplify (11)

$$\Gamma_{A1} = \frac{\partial\varphi_{A2}}{\partial i_{A2}} \cdot \frac{\partial\varphi_{A1}}{\partial\theta_{A1}} - \frac{\partial\varphi_{A1}}{\partial i_{A2}} \cdot \frac{\partial\varphi_{A2}}{\partial\theta_{A2}},$$
$$\Lambda_{A1} = \frac{\partial\varphi_{A1}}{\partial i_{A1}} \cdot \frac{\partial\varphi_{A2}}{\partial i_{A2}} - \frac{\partial\varphi_{A1}}{\partial i_{A2}} \cdot \frac{\partial\varphi_{A2}}{\partial i_{A1}}. \tag{12}$$

Therefore, the differential equation (10) is simplified as (13) shown at the bottom of the next page.

where $\Gamma_{B1}, \Lambda_{B1}, \Gamma_{C1}, \Lambda_{C1}, \Gamma_{A2}, \Lambda_{A2}, \Gamma_{B2}, \Lambda_{B2}, \Gamma_{C2}, \Lambda_{C2}$ are also similar to $\Gamma_{A1}, \Lambda_{A1}$. It can be seen from (13) that the DTPSRM drive under open-circuit operation is developed by the combination of the state and fault functions $\xi_j$ and $\chi_j$.

## IV. DYNAMIC PERFORMANCES OF THE DTPSRM DRIVE

In this section, the above developed model based on MATLAB/Simulink is established to predict the normal and faulty operations of the DTPSRM drive.

### A. *Simulation Model of the DTPSRM Drive*

Several different methods have been proposed for deriving models of SRM, in which the flux linkage or inductance characteristics are modeled by using lookup tables, curve-fitting, or fuzzy logic or artificial neural network from FEA or measurement results. To achieve a good simulation of the DTPSRM, the static flux linkage and torque results of the DTPSRM with SPE and dual-phase excitation, as shown in Figs. 3–5, are used in here. According to the mathematical model (5)–(7), the simulation block diagram of the DTPSRM operation under DCM with the simultaneous TPE ($x1$ and $x2$) and considering mutual coupling between these two phases is presented in Fig. 6.

In order to achieve open-circuit fault-tolerant operations, a fault-tolerant control strategy which is to maintain the rotor speed as the normal operation is performed, as shown in Fig. 7. Under the normal operation, the command speed is usually compared with the sensed speed in speed closed-loop controller to satisfy different load requirements and maintain the speed by adjusting PWM duty cycle. Once one phase is open circuited at some point, it should be immediately shut off or the torque will be reduced with no further action. In order to compensate the lost torque, the most straightforward remedial action is increasing the PWM duty cycle, i.e., the current in healthy phases. This action often happens automatically when the SRM is controlled with a speed closed loop. But if the load torque is large, this method is not enough and not always feasible under some open-circuit fault conditions. In this paper, the angle position control is also employed together with the PWM method for current control to fulfill the load torque and maintain the speed. This alternative method which refers to adjusting the turn-off angle in the healthy phases is adopted except above automatically adjustment. The turn-off delay angle $\Delta\theta_{\mathrm{off}}$ is optimized to increase the turn-off angles in the healthy phases after open-circuit fault, which can improve the dynamic performances such as healthy phase torques, output average torque, and power, and decrease

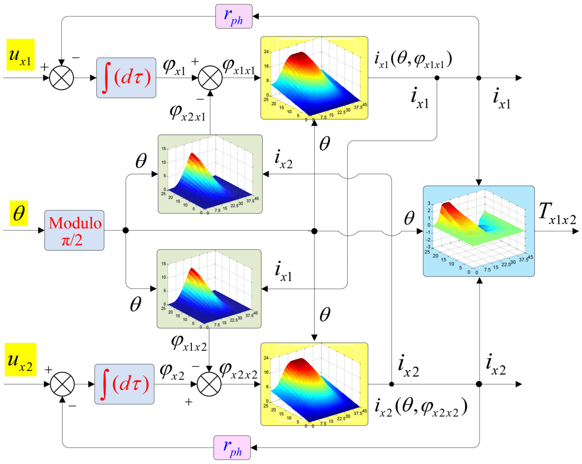

Fig. 6. Simulation block diagram of phases $x1$ and $x2$ of the DTPSRM operation under DCM.

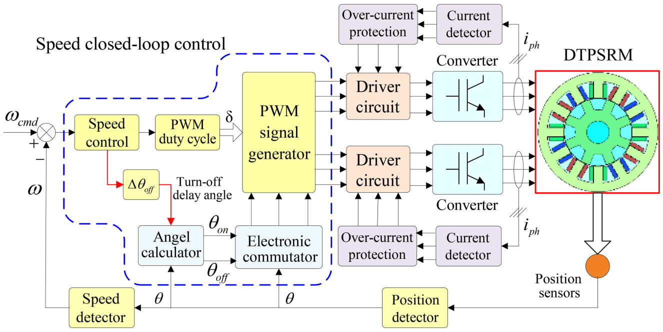

Fig. 7. Fault-tolerant speed closed-loop control for the DTPSRM drive.

---

$$\begin{cases} P_{A1} = P\left(V_{\mathrm{dc}}, \chi_{A1}, \xi_{A1}, i_{A1}, r, \omega, \frac{\partial\varphi_{A1}}{\partial\theta_{A1}}\right) = \chi_{A1} V_{\mathrm{dc}} - \xi_{A1}\left(\omega\frac{\partial\varphi_{A1}}{\partial\theta_{A1}} + r i_{A1}\right) \\ P_j = P\left(V_{dc}, \xi_j, i_j, r, \omega, \frac{\partial\varphi_j}{\partial\theta_j}\right) = -S_j\left(\omega\frac{\partial\varphi_j}{\partial\theta_j} + r i_j\right), j = \text{other phases} \end{cases} \tag{9}$$

---

$$\begin{cases} \frac{di_{A1}}{dt} = F_{A1}(i_{A1}, i_{A2}, V_{\mathrm{dc}}, \theta, \xi_{A1}, \xi_{A2}), & \frac{di_{A2}}{dt} = F_{A2}(i_{A1}, i_{A2}, V_{\mathrm{dc}}, \theta, \xi_{A1}, \xi_{A2}) \\ \frac{di_{B1}}{dt} = F_{B1}(i_{B1}, i_{B2}, V_{\mathrm{dc}}, \theta, \xi_{B1}, \xi_{B2}), & \frac{di_{B2}}{dt} = F_{B2}(i_{B1}, i_{B2}, V_{\mathrm{dc}}, \theta, \xi_{B1}, \xi_{B2}) \\ \frac{di_{C1}}{dt} = F_{C1}(i_{C1}, i_{C2}, V_{\mathrm{dc}}, \theta, \xi_{C1}, \xi_{C2}), & \frac{di_{C2}}{dt} = F_{C2}(i_{C1}, i_{C2}, V_{\mathrm{dc}}, \theta, \xi_{C1}, \xi_{C2}) \end{cases} \tag{10}$$

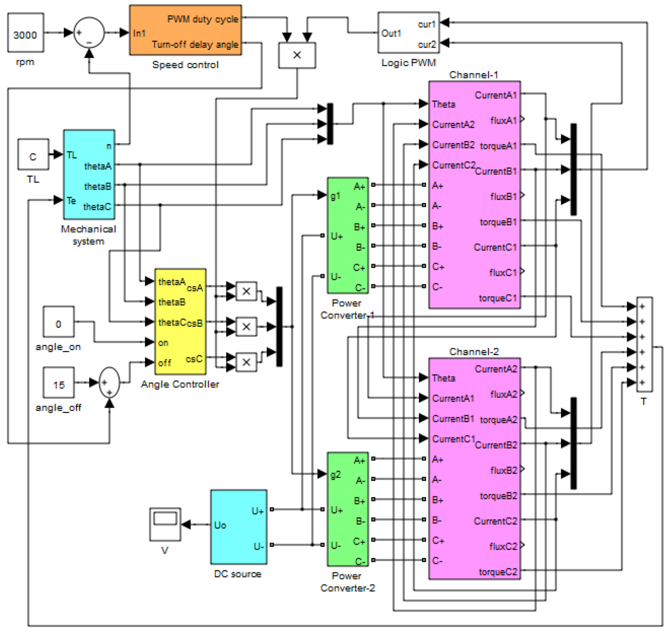

Fig. 8. Whole Simulink model of the DTPSRM drive system.

the torque ripple under open-phase fault-tolerant operations. After that, the switching signals are produced to control the power converter through the PWM generator and electric commutator by adjusting the PWM duty cycle. Thus, the rotor speed is regulated in a closed loop. This alternative method which refers to adjusting the turn-off angle with PWM method is also appropriate for the normal operation with large load torque. However, the optimized turn-off angle under normal operation will be smaller than that under fault operation because the number of working phases is more than that of the fault condition.

The whole simulation system of the DTPSRM drive based on MATLAB/Simulink is shown in Fig. 8, which consists of the dual three-phase winding models, speed controller, two asymmetric half-bridge converters, logic PWM, angle controller, mechanical system and dc source, etc. It should be noted that the dual three-phase winding models mainly conclude the self- and mutual flux linkages, and torque characteristics.

### *B. Normal Performances and Model Verification*

Fig. 9 shows simulated dynamic performance of speed step response with closed-loop control for a 0.5-N·m load at normal condition. The input dc-link voltage and command rotor speed are fixed at 30 V and set to 3000 r/min, and the turn-on and turn-off angles are fixed at 0° and 15°, respectively. In order to validate the developed model of the DTPSRM drive based on MATLAB/Simulink, Fig. 10(a) and (b) compares the steady-state phase voltage, current, and dc-link current in one channel obtained via simulation and experiment when the DTPSRM drive operates under the speed closed-loop control at the same condition of 3000 r/min. Another validation is done for the DTPSRM running with a speed of 3000 r/min under single-pulse control. In this case, the dc-link voltage was 25 V. Simulated and measured phase currents in two channels are shown in Fig. 11. It can be seen that the simulated waveforms matches the experimental results quite well, which validate the accuracy of the developed model and analysis.

Furthermore, in order to investigate the effect of different turn-off angles for the output performance of the DTPSRM drive, Fig. 12 shows the profiles of phase current and phase torque and total torque waveforms of the DTPSRM over one electrical cycle under single-pulse control, varying the turn-off angle. The dc-link voltage and the rotor speed of the motor are fixed at 30 V and 3000 r/min respectively, and the turn-on angle is set at 0° in this simulation. Each current profile shown is for a different turn-off angle—from 10° to 20° at 2.5° intervals. Table IV gives the output dynamic performance with different turn-off angles under single-pulse operation. It can be seen that the RMS phase current, phase torque, output average torque,

---

$$F_{A1} = \frac{di_{A1}}{dt} = \frac{\xi_{A2}\frac{\partial\varphi_{A2}}{\partial i_{A2}}P_{A1} - \xi_{A1}\frac{\partial\varphi_{A1}}{\partial i_{A2}}P_{A2}}{\xi_{A1}\xi_{A2}\left(\frac{\partial\varphi_{A1}}{\partial i_{A2}}\cdot\frac{\partial\varphi_{A2}}{\partial i_{A1}} - \frac{\partial\varphi_{A1}}{\partial i_{A1}}\cdot\frac{\partial\varphi_{A2}}{\partial i_{A2}}\right)}$$
$$= \frac{\left(K_{A1}\xi_{A2}\frac{\partial\lambda_{A2}}{\partial i_{A2}} - \xi_{A1}\frac{\partial\lambda_{A1}}{\partial i_{A2}}\right)V_{\mathrm{dc}} - \xi_{A1}\xi_{A2}\left[\omega\left(\frac{\partial\varphi_{A2}}{\partial i_{A2}}\cdot\frac{\partial\varphi_{A1}}{\partial\theta_{A1}} - \frac{\partial\varphi_{A1}}{\partial i_{A2}}\cdot\frac{\partial\varphi_{A2}}{\partial\theta_{A2}}\right) - r\left(\frac{\partial\varphi_{A2}}{\partial i_{A2}} - \frac{\partial\varphi_{A1}}{\partial i_{A2}}\right)(i_{A1} - i_{A2})\right]}{\xi_{A1}\xi_{A2}\left(\frac{\partial\varphi_{A1}}{\partial i_{A1}}\cdot\frac{\partial\varphi_{A2}}{\partial i_{A2}} - \frac{\partial\varphi_{A1}}{\partial i_{A2}}\cdot\frac{\partial\varphi\lambda_{A2}}{\partial i_{A1}}\right)} \tag{11}$$

---

$$\begin{cases}
\frac{di_{A1}}{dt} = \frac{r}{\Lambda_{A1}}\left(\frac{\partial\varphi_{A2}}{\partial i_{A2}} - \frac{\partial\varphi_{A1}}{\partial i_{A2}}\right)(i_{A1} - i_{A2}) + \left(\frac{\chi_{A1}}{\xi_{A1}}\frac{\partial\varphi_{A2}}{\partial i_{A2}} - \frac{1}{\xi_{A2}}\frac{\partial\varphi_{A1}}{\partial i_{A2}}\right)\frac{V_{\mathrm{dc}}}{\Lambda_{A1}} - \omega\frac{\Gamma_{A1}}{\Lambda_{A1}} \\
\frac{di_{B1}}{dt} = \frac{r}{\Lambda_{B1}}\left(\frac{\partial\varphi_{B2}}{\partial i_{B2}} - \frac{\partial\varphi_{B1}}{\partial i_{B2}}\right)(i_{B1} - i_{B2}) + \left(\frac{1}{\xi_{B1}}\frac{\partial\varphi_{B2}}{\partial i_{B2}} - \frac{1}{\xi_{B2}}\frac{\partial\varphi_{B1}}{\partial i_{B2}}\right)\frac{V_{\mathrm{dc}}}{\Lambda_{B1}} - \omega\frac{\Gamma_{B1}}{\Lambda_{B1}} \\
\frac{di_{C1}}{dt} = \frac{r}{\Lambda_{C1}}\left(\frac{\partial\varphi_{C2}}{\partial i_{C2}} - \frac{\partial\varphi_{C1}}{\partial i_{C2}}\right)(i_{C1} - i_{C2}) + \left(\frac{1}{\xi_{C1}}\frac{\partial\varphi_{C2}}{\partial i_{C2}} - \frac{1}{\xi_{C2}}\frac{\partial\varphi_{C1}}{\partial i_{C2}}\right)\frac{V_{\mathrm{dc}}}{\Lambda_{C1}} - \omega\frac{\Gamma_{C1}}{\Lambda_{C1}} \\
\frac{di_{A2}}{dt} = \frac{r}{\Lambda_{A2}}\left(\frac{\partial\varphi_{A1}}{\partial i_{A1}} - \frac{\partial\varphi_{A2}}{\partial i_{A1}}\right)(i_{A2} - i_{A1}) + \left(\frac{1}{\xi_{A2}}\frac{\partial\varphi_{A1}}{\partial i_{A1}} - \frac{\chi_{A1}}{\xi_{A1}}\frac{\partial\varphi_{A2}}{\partial i_{A1}}\right)\frac{V_{\mathrm{dc}}}{\Lambda_{A2}} - \omega\frac{\Gamma_{A2}}{\Lambda_{A2}} \\
\frac{di_{B2}}{dt} = \frac{r}{\Lambda_{B2}}\left(\frac{\partial\varphi_{B1}}{\partial i_{B1}} - \frac{\partial\varphi_{B2}}{\partial i_{B1}}\right)(i_{B2} - i_{B1}) + \left(\frac{1}{\xi_{B2}}\frac{\partial\varphi_{B1}}{\partial i_{B1}} - \frac{1}{\xi_{B1}}\frac{\partial\varphi_{B2}}{\partial i_{B1}}\right)\frac{V_{\mathrm{dc}}}{\Lambda_{B2}} - \omega\frac{\Gamma_{B2}}{\Lambda_{B2}} \\
\frac{di_{C2}}{dt} = \frac{r}{\Lambda_{C2}}\left(\frac{\partial\varphi_{C1}}{\partial i_{C1}} - \frac{\partial\varphi_{C2}}{\partial i_{C1}}\right)(i_{C2} - i_{C1}) + \left(\frac{1}{\xi_{C2}}\frac{\partial\varphi_{C1}}{\partial i_{C1}} - \frac{1}{\xi_{C1}}\frac{\partial\varphi_{C2}}{\partial i_{C1}}\right)\frac{V_{\mathrm{dc}}}{\Lambda_{C2}} - \omega\frac{\Gamma_{C2}}{\Lambda_{C2}}
\end{cases} \tag{13}$$

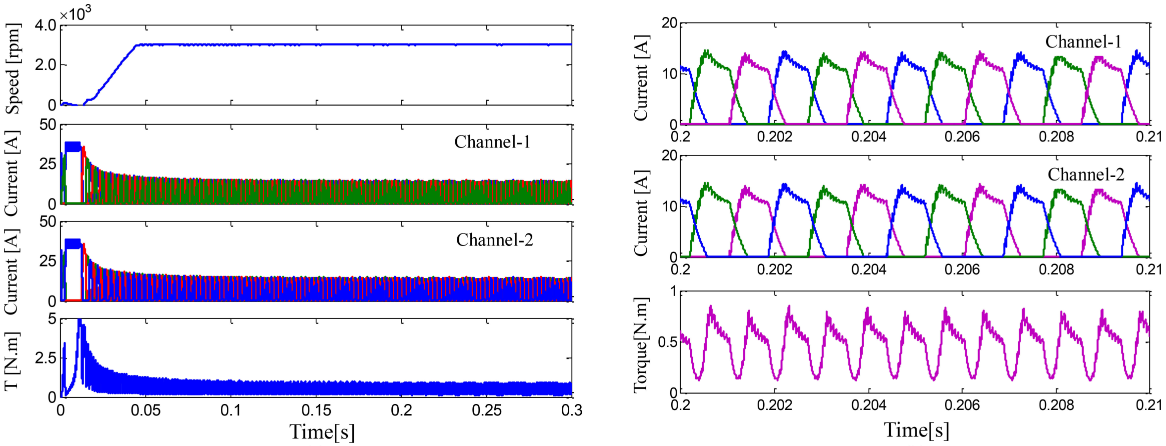

(a) (b)

Fig. 9. Simulated dynamic performance of speed step response with closed-loop control at normal condition. (a) Transient speed, phase currents and torque. (b) Steady-state phase currents in channels 1 and 2 and total torque waveforms.

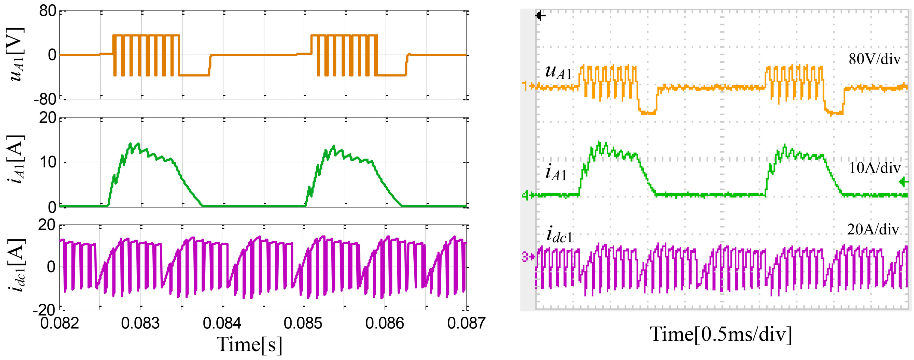

(a) (b)

Fig. 10. (a) Simulated and (b) measured steady-state phase voltage, current, and dc-link current in channel 1 at 3000 r/min with closed-coop control.

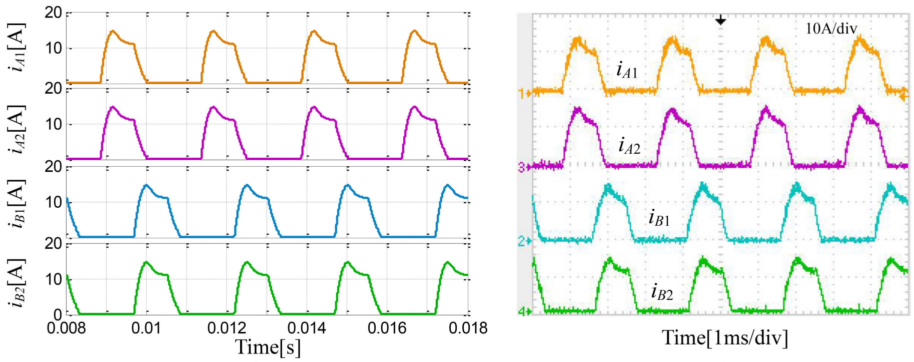

(a) (b)

Fig. 11. (a) Simulated and (b) measured steady-state phase currents in channels 1 and 2 with single-pulse control at normal condition.

and output power of the DTPSRM drive increase with the turn-off angle increased, whereas the torque ripple decreases with the turn-off angle increased. So the turn-off angle $\theta_{\text{off}}$ can be delayed for optimization to improve the performances of healthy phase torque, output average torque, and power, and decrease the torque ripple under open-phase fault-tolerant operation. It should be noted that this optimization is also for all the healthy phases in both channels under fault-tolerant operation.

### *C. Open-Phase Performances Under Single-Pulse Operation*

Owing to the redundant configuration in the DTPSRM, it possess high fault-tolerant feature. A faulty phase can be cut off in the event of open-circuit fault, and the remaining healthy phases will continue to operate with reduced power if the system does not take any remedial action. In order to investigate this faulty characteristic and the mutual coupling effect between each channel of the DTPSRM drive under open-phase conditions, the

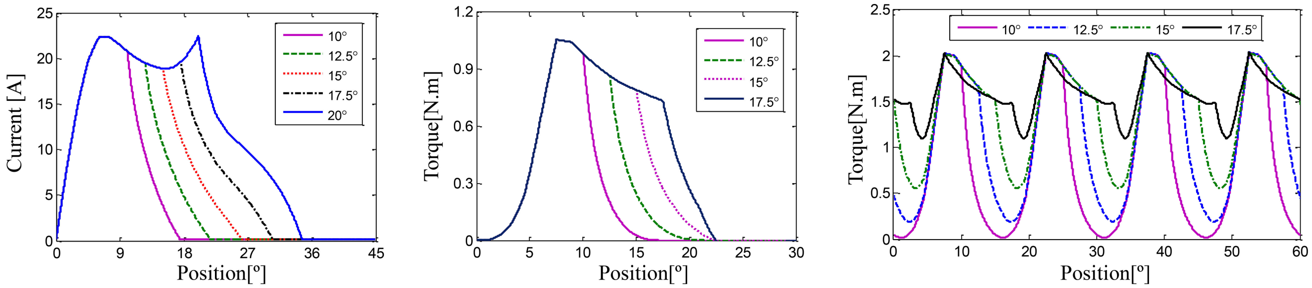

(a) (b) (c)

Fig. 12. Sets of simulated (a) phase current, (b) phase torque, and (c) total torque traces obtained by varying the turn-off angle positions.

TABLE IV
DYNAMIC PERFORMANCE WITH DIFFERENT TURN-OFF ANGLES UNDER SINGLE-PULSE OPERATION

| Parameter | $\theta_{\rm on} = 0°$ | | | |
|---|---|---|---|---|
| | $\theta_{\rm off} = 10°$ | $\theta_{\rm off} = 12.5°$ | $\theta_{\rm off} = 15°$ | $\theta_{\rm off} = 17.5°$ |
| RMS phase current, A | 5.048 | 6.397 | 7.783 | 9.284 |
| Average torque, N·m | 0.826 | 1.151 | 1.435 | 1.623 |
| Torque ripple | 160.3% | 154.6% | 105.9% | 50.6% |
| Output Power, W | 259.5 | 361.6 | 450.8 | 509.9 |

above developed simulation model is used to predict the faulty steady-state performances of the remaining healthy phases under lack of one and multi phases with single-pulse control.

First, Fig. 13 shows the simulated output faulty performances of the DTPSRM drive under lack of one phase (A1), two phases (A1, A2 and A1, B1), and three-phases (A1, B1, C1) with single-pulse operation. In these simulations, the dc-link voltage and the speed are also fixed at 30 V and 3000 r/min, and the turn-on and turn-off angles are fixed at 0° and 15°, respectively. It should be noted that the speed of the machine is fixed at 3000 r/min, which means that all simulations were performed at a constant imposed speed of 3000 r/min in the simulation model. The main focus is to investigate the torque production capability of the DTPSRM under diverse winding fault conditions with single-pulse control. For example, when one phase is faulted still $3 + 2$ phases of the machine are working (the 83.3% of the machine's windings). The remaining healthy phases are still contributing to the torque generation, but of lower values. Table V gives some summaries of the predicted faulty steady-state performances such as the produced average torque, torque ripple, output power, copper loss, copper loss per torque, and efficiency during lack of one and multiphases with single-pulse control at 3000 r/min. It can be found that the developed average torques of the DTPSRM under lack of one phase (A1) and two phases (A1 and A2) conditions are about 1.179 and 0.955 N·m, which are 82.2% and 66.6% of the normal operation torque. The torque ripple under lack of phases A1 and A2 is 219.2%, which is the maximum in all of the four open-phase faults. The efficiencies under lack of phases are lower than that under normal operation.

Furthermore,Fig. 14 shows the developed average torque versus speed and copper loss per torque characteristics of the DTPSRM drive with the same dc-link voltage under the normal and various open-phase conditions. It can be seen that the output average torques under both normal and open-phase conditions decrease with the rotor speed increased. Moreover, the developed average torque under normal DCM operation is more than two times of that under single-channel operation mode, i.e., during loss of three phases (A1, B1, and C1), and the copper losses per torque under normal and two-phase (A1 and A2) open-circuit conditions are almost the same, which are the lowest in all of the four open-phase faults.

### D. *Fault-Tolerant Performance Under Closed-Loop Control*

Fig. 15 shows the simulated speed and all phase currents responses of the DTPSRM drive operation with one-phase (A1) open-circuit under the fault-tolerant control. The simulation condition was performed using the same setting as that of aforementioned. As expected, the rotor speed of the DTPSRM drive is able to keep the command speed of 3000 r/min and the currents in healthy phases increased under the fault-tolerant control after the phase A1 is open circuited. Furthermore, it can be observed that the current amplitude of phase A2 is larger more than the other healthy phase currents because there is no mutual coupling in phase A2 during loss of phase A1.

Fig. 16 shows the simulated speed and all phase currents responses of the DTPSRM drive operation with two-phase (A1 and A2) open-circuit under the fault-tolerant control. It is evident that the corresponding faulty phase currents drop to zero after they are open circuited simultaneously. However, the DTPSRM is still able to keep the command speed under the fault-tolerant control. Furthermore, it can be noted that the healthy phase currents of C1 and C2 in both channels 1 and 2 are slightly larger than those of B1 and B2. However, the healthy phase currents of B1 and B2 almost keep the same with each other, and the healthy phase currents of C1 and C2 also keep the same.

Furthermore, Fig. 17 shows the simulated speed and all phase currents of the DTPSRM drive operation with three-phase (A1, B1, C1) open-circuit under the fault-tolerant control. It can also be seen that the DTPSRM is still able to maintain the command speed as the normal operation.

## V. EXPERIMENTAL VERIFICATION

In this section, the experimental drive platform of the prototype 12/8-pole DTPSRM is set up, as shown in Fig. 18, and

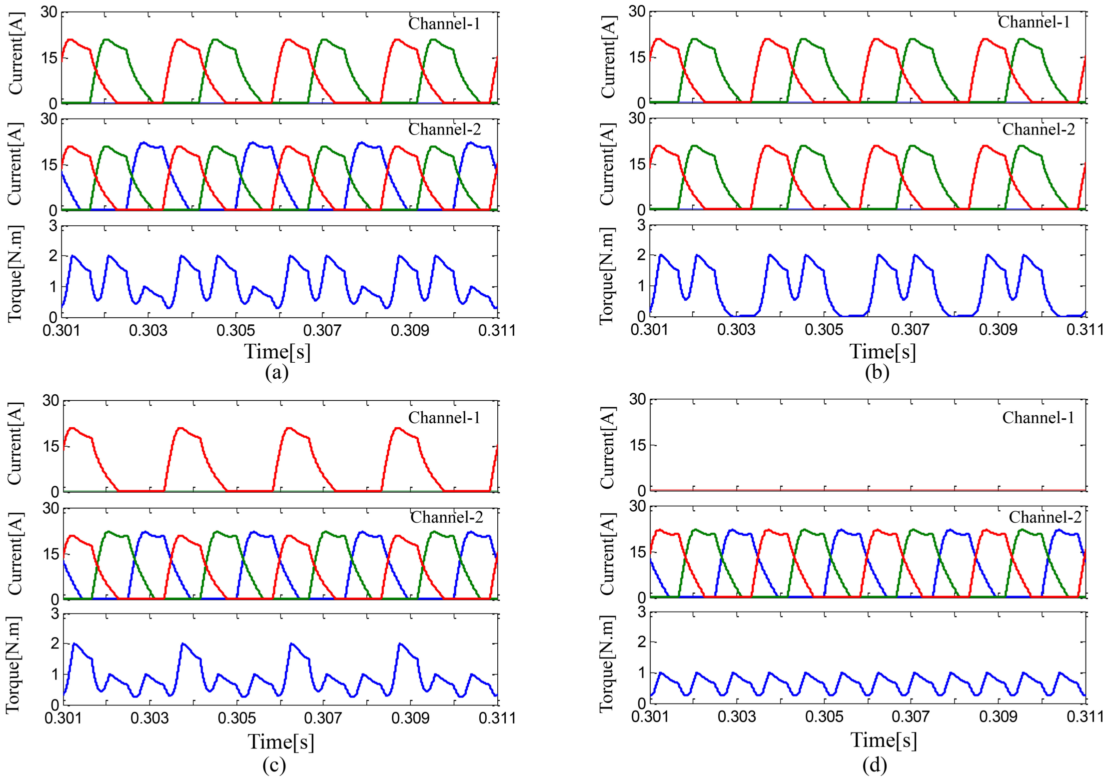

(a)

(b)

(c)

(d)

Fig. 13. Simulated steady-state performances with different open-circuit faults under single-pulse control. (a) Phase A1 open circuited. (b) Phases A1 and A2 open circuited. (c) Phases A1 and B1 open circuited. (d) Phases A1, B1, and C1 open circuited.

TABLE V
Summary of the Predicted Normal and Faulty Performances with Single-Pulse Control at 3000 r/min

| Condition | Normal | A1 opened | A1 and A2 opened | A1 and B1 opened | A1, B1, and C1 opened |
|---|---|---|---|---|---|
| Sum of RMS phase current, A | $7.783 \times 6$ | $7.783 \times 4 + 8.715$ | $7.783 \times 4$ | $7.783 \times 2 + 8.758 \times 2$ | $8.775 \times 3$ |
| Average torque, N·m | 1.435 | 1.179 | 0.955 | 0.926 | 0.670 |
| Percentage of normal torque | 100% | 82.2% | 66.6% | 64.5% | 46.6% |
| Torque ripple | 105.9% | 150.5% | 219.2% | 197.4% | 118.5% |
| Output Power, W | 450.8 | 370.4 | 300.0 | 290.9 | 210.5 |
| Copper loss, W | 61.78 | 54.10 | 41.19 | 46.67 | 39.27 |
| Copper loss per torque, W/N·m | 43.05 | 45.88 | 43.13 | 50.39 | 58.61 |

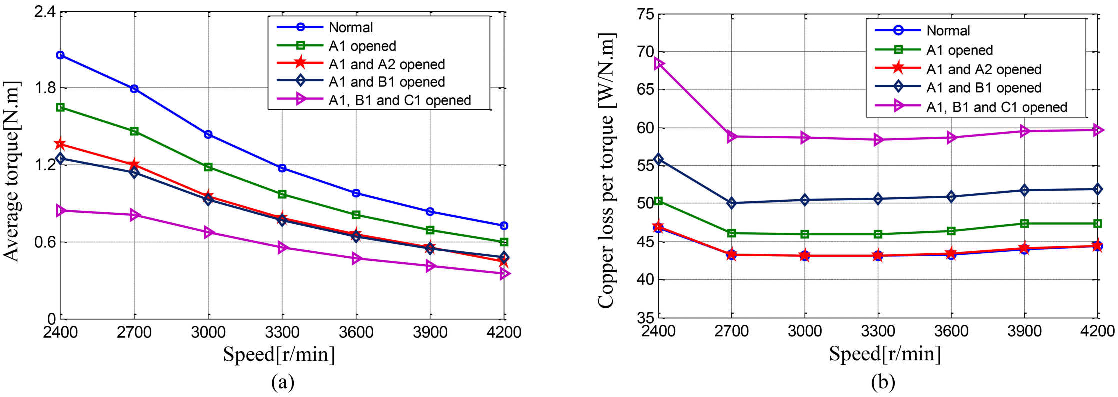

(a)

(b)

Fig. 14. (a) Average torque–speed and (b) copper loss per torque characteristics under lack of diverse-phase operations.

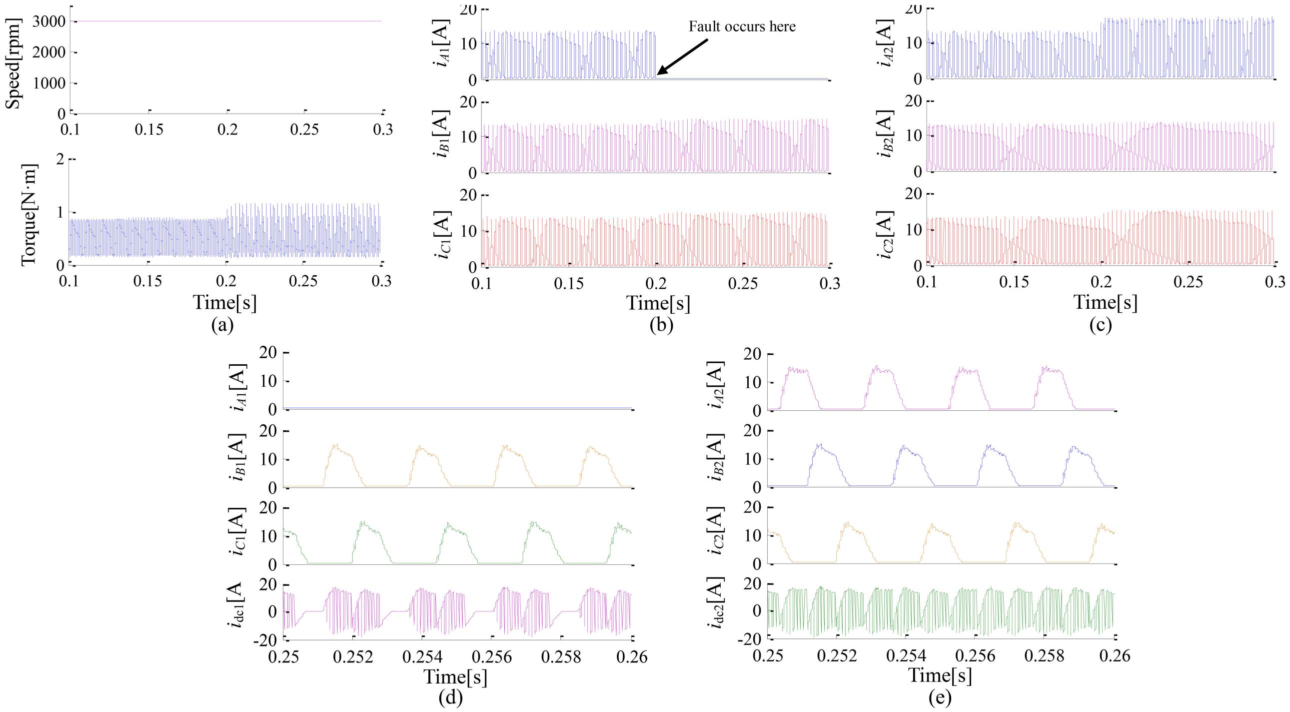

Fig. 15. Simulated waveforms at fault-tolerant operation when phase A1 is open circuited. (a) Rotor speed, (b) and (c) transient phase currents in channels 1 and 2, (d) and (e) steady-state phase currents in channels 1 and 2 after fault.

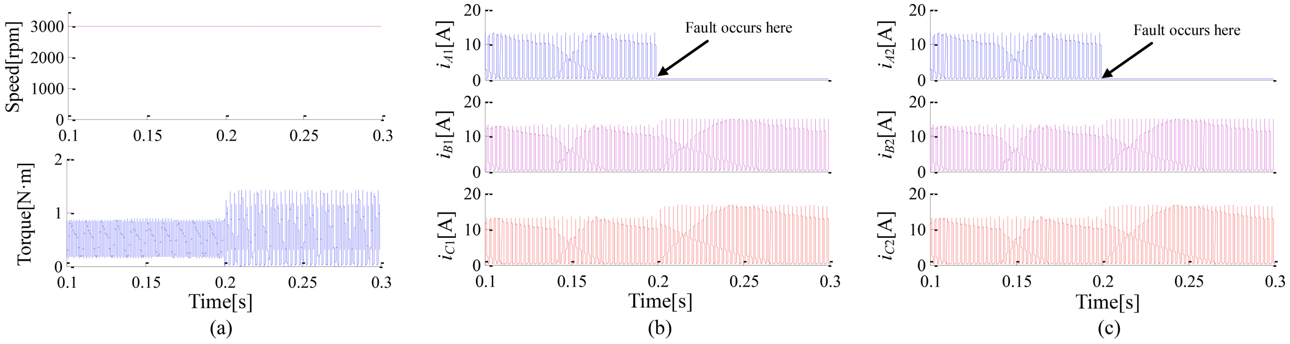

Fig. 16. Simulated waveforms at fault-tolerant operation when phases A1 and A2 are open circuited. (a) Rotor speed. (b) and (c) phase currents in channels 1 and 2.

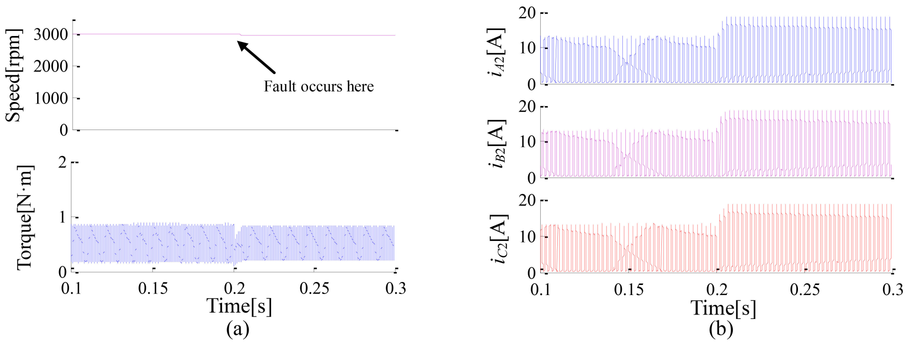

Fig. 17. Simulated waveforms at fault-tolerant operation when phases A1, B1, and C1 are open circuited. (a) Rotor speed. (b) Phase currents in channel 2.

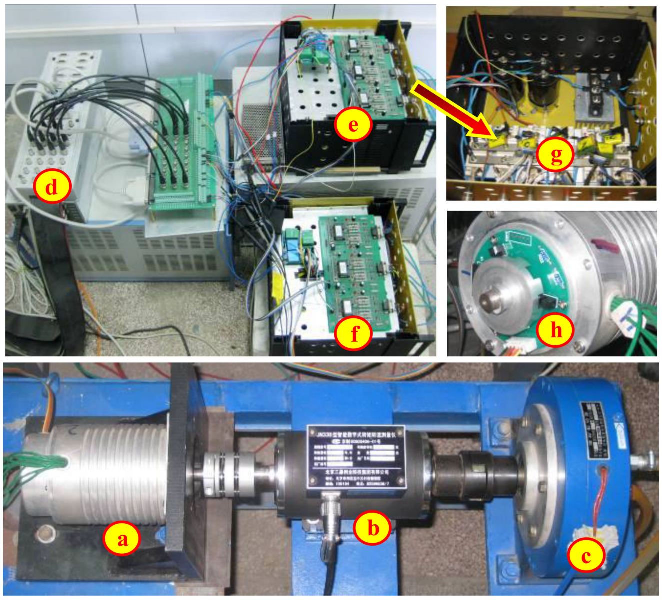

Fig. 18. Experimental setup: (a) DTPSRM, (b) torque transducer, (c) hysteresis brake, (d) dSPACE 1104, (e), (f) driver circuits in channels 1 and 2, (g) asymmetric power converter in one channel, and (h) rotor position sensor.

the normal and open-circuit fault operations are tested to verify the above analysis, simulation, and fault-tolerant control strategy. The DTPSRM is loaded using a hysteresis brake coupled through a torque transducer. The main control system is implemented by dSPACE 1104 which is used for developing control programs and the PWM switching signals are transmitted to the gate drivers. The dual three-phase channels of the DTPSRM are connected to two separate asymmetric three-phase half-bridge circuit units, which are used as the dual-channel power converters.

### A. Normal Operation With Closed-Loop Control

First, the speed step response of the DTPSRM drive under normal DCM operation with speed closed-loop control is performed, as shown in Fig. 19. During this operation, the command speed is set to 3000 r/min; the other experiment conditions were performed using the same setting as those of the aforementioned simulation. As expected, the DTPSRM accelerate quickly from standstill to 3000 r/min and the phase currents in two channels are almost kept the same and synchronous, which verified the speed closed-loop control strategy.

### B. Faulty Operation With Single-Pulse Control

Second, the output transient average torque characteristics of the DTPSRM drive under normal and lack of diverse phases operations with single-pulse control were measured, as shown in Table VI. In each case, the dc-link voltage is fixed at 30 V and the speed is maintained at 3000 r/min by adjusting the voltage of the hysteresis brake, which is used to change the load torque. The output average torque of the DTPSRM is equal to the load torque and determined by load characteristics of the hysteresis brake at steady-state operation, then the developed torque of the machine is measured by means of a torque transducer. These tests were performed for the same conditions as those carried out during the simulations. As can be seen in Table VI, the simulated average torques is quite close to those obtained by measurements. The relative errors between the simulated and measured data are significantly under 7%, which verified the aforementioned analysis and simulation again.

TABLE VI
AVERAGE TORQUE CHARACTERISTICS WITH SINGLE-PULSE CONTROL AT DIFFERENT CONDITIONS

| Condition | Normal | A1 opened | A1 and A2 opened | A1 and B1 opened | A1, B1 and C1 opened |
|---|---|---|---|---|---|
| Simulated torque, N·m | 1.435 | 1.179 | 0.955 | 0.926 | 0.670 |
| Measured torque, N·m | 1.346 | 1.107 | 0.893 | 0.862 | 0.624 |
| Relative error | 6.20% | 6.11% | 6.49% | 6.91% | 6.87% |

### C. Fault-Tolerant Performances Under Open-Circuit Faults

First, Fig. 20 shows the measured fault-tolerant performance during the single- phase (A1) open-circuit occurrence at 3000 r/min. As expected, the speed is maintained before and after the failure under the fault-tolerant control. The current amplitude of phase A2 is larger more than the other healthy phase currents. Second, Figs. 21 and 22 show the measured fault-tolerant performances when two phases (A1, B1 and A1, A2) in one channel and two channels are open circuited, respectively. It can be observed that the speed after two-phase open-circuit is still maintained. Third, Fig. 23 shows the measured fault-tolerant performances when the three phases in one channel, namely, phases A1, B1, and C1, are open circuited. It can be seen that the DTPSRM drive after three-phase open-circuit still be able to maintain the command speed. It can be concluded that the DTPSRM drive under diverse open-circuit fault-tolerant operations can be able to maintain the command speed as the normal operation, which verified the fault-tolerant control strategy. Furthermore, it can be seen from Fig. 1(c) that there is a filter circuit in the supply side of the dc bus. In the practical filter circuit of the DTPSRM drive, a HCG FA capacitor of 6600 $\mu$F/450 V is connected across the dc link. Owing to the large capacitor, the dc link is almost like a constant dc power supply, and the dc-link voltage pulsation is very small under normal and faulty conditions.

### D. Self-Starting Capability Under Open Circuits

Finally, the self-starting capability of the DTPSRM drive under diverse open-circuit faults is investigated in this paper. Fig. 24 shows the startup responses under normal and lack of one- and two-phase operations with single-pulse control (open loop), respectively. It can be seen that the motor drive can reach steady-state speed of 4300 r/min at normal condition, while it can only reach 4000 r/min and 3750 r/min under lack of one- and two-phase conditions. Furthermore, it can be found that the rise up times of the DTPSRM drive under normal and lack of one- and two-phase operations are 0.75, 0.85, and 1.06 s, respectively.

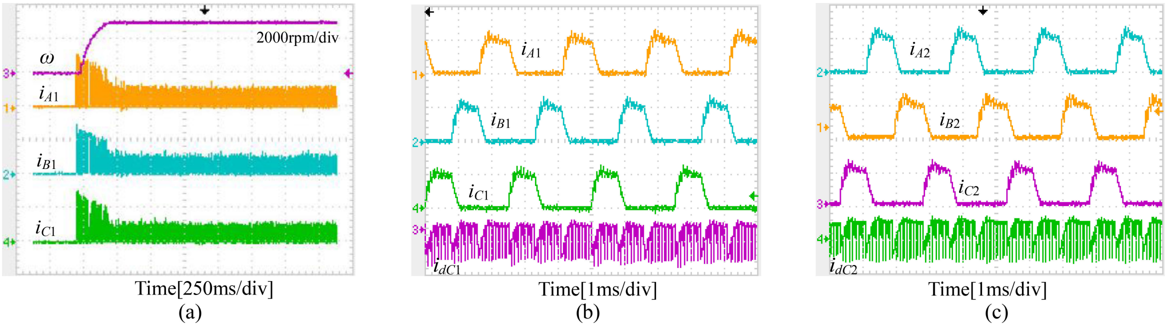

Fig. 19. Speed step response with closed-loop control at normal condition. (a) Transient speed response and currents in channel 1. (b) and (c) Steady-state current waveforms in channels 1 and 2.

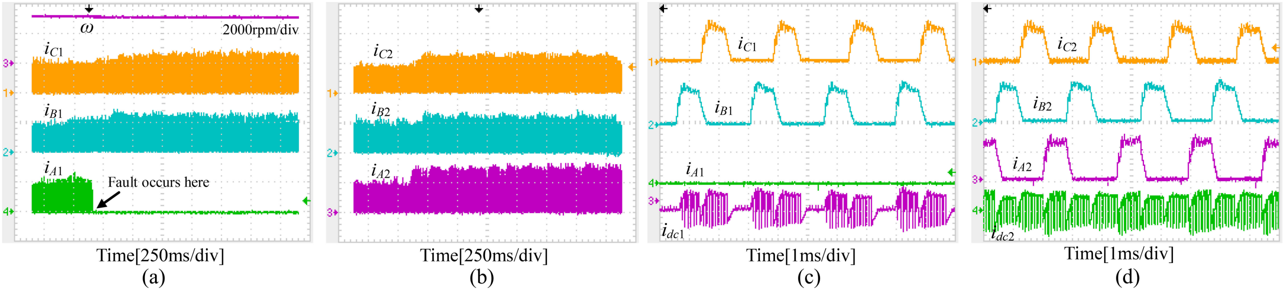

Fig. 20. Fault-tolerant performance of one-phase (A1) open-circuit. (a) and (b) Transient speed and currents in channels 1 and 2. (c) and (d) Zoomed-in views of steady-state current waveforms in two channels after fault.

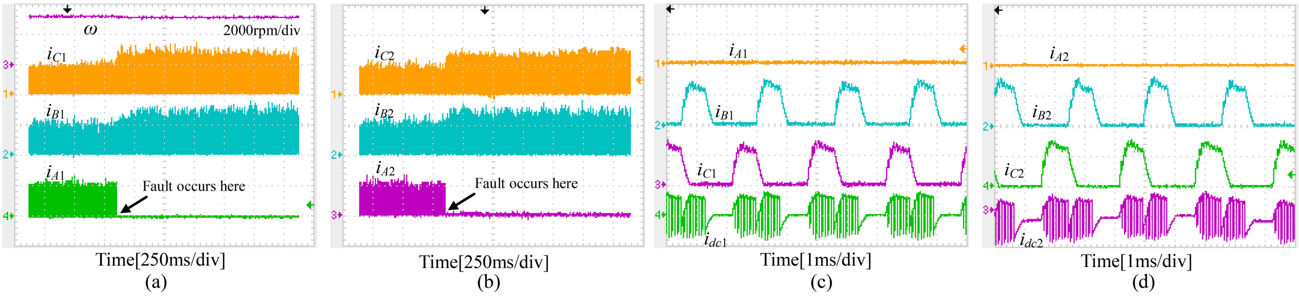

Fig. 21. Fault-tolerant performance of two-phase (A1 and A2) open-circuit. (a) and (b) Transient speed and currents in channels 1 and 2. (c) and (d) Zoomed-in views of steady-state current waveforms in two channels.

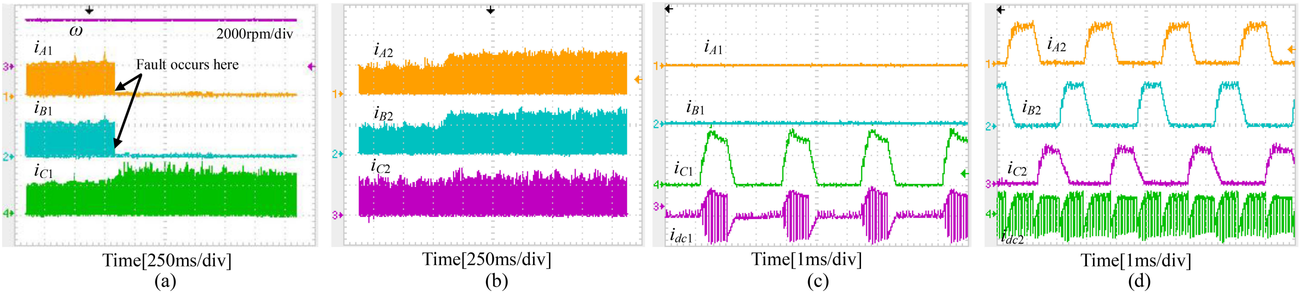

Fig. 22. Fault-tolerant performance of two-phase (A1 and B1) open-circuit. (a) and (b) Transient speed and currents in channels 1 and 2. (c) and (d) Zoomed-in views of steady-state current waveforms in two channels.

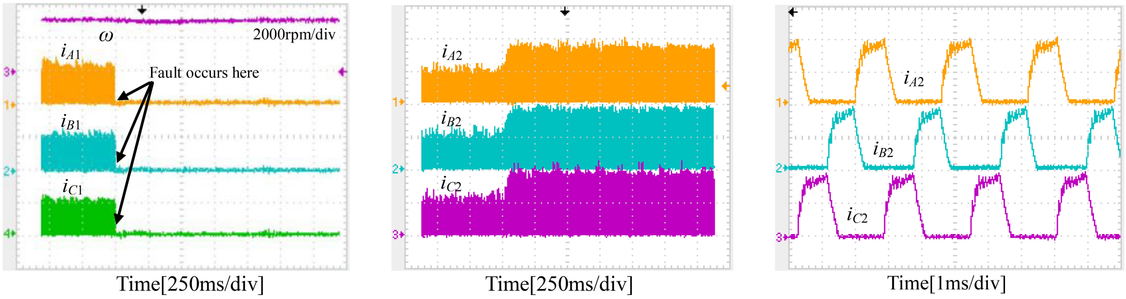

(a) (b) (c)

Fig. 23. Fault-tolerant performance of three-phase (A1, B1, and C1) open-circuit. (a) and (b) Transient speed and currents in channels 1 and 2. (c) Zoomed-in views of steady-state current waveforms in channel 2.

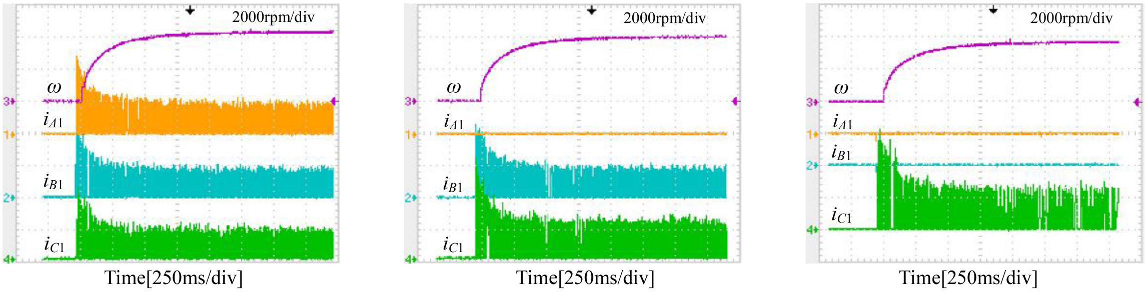

(a) (b) (c)

Fig. 24. Measured speed and current responses at startup under open-loop control. (a) Normal operation. (b) Lack of one-phase (A1) operation. (c) Lack of two-phase (A1 and B1) operation.

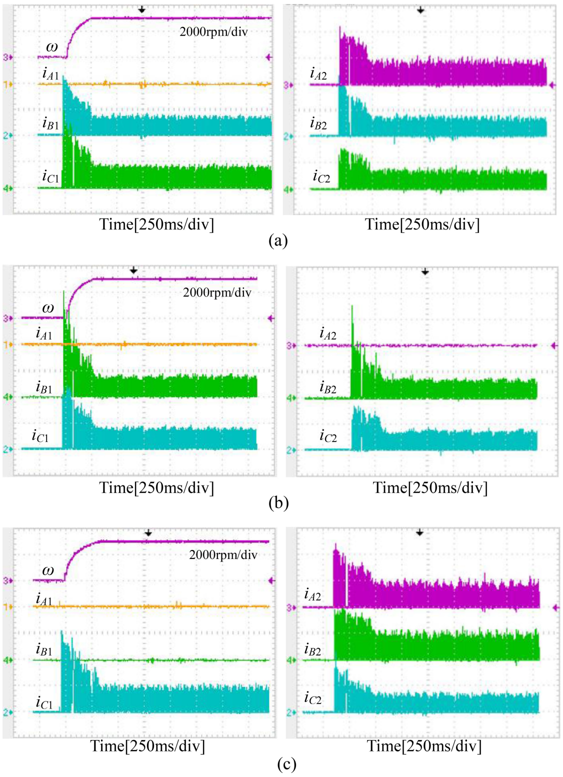

Fig. 25. Measured speed and current responses at startup under fault-tolerant closed-loop control. (a) Lack of one-phase (A1) operation. (b) Lack of two-phase (A1 and A2) operation. (c) Lack of two-phase (A1 and B1) operation.

Furthermore, Fig. 25 shows the startup responses under normal and lack of one- and two-phase operations with fault-tolerant speed closed-loop control, respectively. During these operations, the command speed is still set to 3000 r/min. It confirms that the DTPSRM drive can still successfully perform self-starting and quickly reach the command speed under lack of one- and two-phase operations with fault-tolerant closed-loop control. Moreover, it can be seen from Figs. 19(a) and 25 that the rise up time of the DTPSRM drive under normal operation is shorter than that under lack of one- and two-phase operations.

## VI. CONCLUSION

This paper has analyzed and investigated the fault-tolerant characteristics of a mutually coupled DTPSRM drive under various open-circuit fault operations. From the analysis and simulations, it is confirmed that: 1) the dual three-phase winding units in the DTPSRM would have strong magnetic coupling when they are excited simultaneously and operating under DCM; 2) the average and maximum torques developed with TPE are larger than two times of that with SPE at the same current; 3) the output average torques under both normal and open-phase conditions decrease with the rotor speed increased; 4) the developed average torques of the DTPSRM under lack of one and two phases conditions are still be able to develop 82.2% and 66.6% of the normal operation torque, and the torque ripple under lack of two phases (in one channel) operation is the maximum in all of open-phase faults; and 5) the efficiencies under lack of phases are lower than that under normal operation. Finally, an experimental drive platform of the prototype 12/8-pole DTPSRM is set up. Both simulation and experiment show that the DTPSRM drive can still be able to maintain the command speed with one-, two- and three-phase open-circuit fault-tolerant operations, and the DTPSRM drive can also successfully perform self-starting under lack of one- and two-phase operations with the fault-tolerant control. This fault-tolerant mutually coupled DTPSRM would have a wide future in some safety-critical applications such as MEA and EV/HEV applications.

## REFERENCES

[1] A. Mohammadpour and L. Parsa, "A unified fault-tolerant current control approach for five-phase PM motors with trapezoidal back EMF under different stator winding connections," *IEEE Trans. Power Electron.*, vol. 28, no. 7, pp. 3517–3527, Jul. 2013.

[2] I. Jeong, B. J. Hyon, and K. Nam, "Dynamic modeling and control for SPMSMs with internal turn short fault," *IEEE Trans. Power Electron.*, vol. 28, no. 7, pp. 3495–3503, Jul. 2013.

[3] B. G. Gu, J. H. Choi, and I. S. Jung, "Development and analysis of inter-turn short fault model of PMSMs with series and parallel winding connections," *IEEE Trans. Power Electron.*, vol. 29, no. 4, pp. 2016–2026, Apr. 2014.

[4] S. M. Jung, J. S. Park, H. W. Kim, K. Y. Cho, and M. J. Youn, "An MRAS-based diagnosis of open-circuit fault in PWM voltage-source inverters for PM synchronous motor drive systems," *IEEE Trans. Power Electron.*, vol. 28, no. 5, pp. 2514–2527, Mar. 2013.

[5] W. X. Zhao, M. Cheng, X. Y. Zhu, and W. Hua, "Analysis of fault-tolerant performance of a doubly salient permanent-magnet motor drive using transient cosimulation method," *IEEE Trans. Ind. Electron.*, vol. 55, no. 4, pp. 1739–1748, Apr. 2008.

[6] W. X. Zhao, K. T. Chau, M. Cheng, J. H. Ji, and X. Y. Zhu, "Remedial brushless AC operation of fault-tolerant doubly salient permanent-magnet motor drives," *IEEE Trans. Ind. Electron.*, vol. 57, no. 6, pp. 2134–2141, Jun. 2010.

[7] W. X. Zhao, M. Cheng, W. Hua, and H. Y. Jia, "Back-EMF harmonic analysis and fault-tolerant control of flux switching permanent-magnet machine with redundancy," *IEEE Trans. Ind. Electron.*, vol. 58, no. 5, pp. 1926–1935, May 2011.

[8] W. X. Zhao, M. Cheng, K. T. Chau, and R. W. Cao, "Remedial injected-harmonic-current operation of redundant flux switching permanent-magnet motor drives," *IEEE Trans. Ind. Electron.*, vol. 60, no. 1, pp. 151–159, Jan. 2011.

[9] R. Kianinezhad, B. Nahid-Mobarakeh, L. Baghli, F. Betin, and G.-A. Capolino, "Modeling and control of six-phase symmetrical induction machine under fault condition due to open phases," *IEEE Trans. Ind. Electron.*, vol. 55, no. 5, pp. 1966–1977, May 2008.

[10] R. Kianinezhad, R. Alcharea, B. Nahid, F. Betin, and G. A. Capolino, "Analysis and evaluation of DTC and FOC in open phase fault operation of six-phase induction machines," in *Proc. 14th IEEE Mediterr. Electrotech. Conf.*, Ajaccio, France, May 5–7, 2008, pp. 447–452.

[11] M. A. Abbas, R. Christen, and T. M. Jahns, "Six-phase voltage source inverter driven induction motor," *IEEE Trans. Ind. Appl.*, vol. IA-20, no. 5, pp. 1251–1259, Sep./Oct. 1984.

[12] R. Bojoi, F. Farina, G. Griva, F. Profumo, and A. Tenconi, "Direct torque control for dual three-phase induction motor drives," *IEEE Trans. Ind. Appl.*, vol. 41, no. 6, pp. 1627–1636, Nov./Dec. 2005.

[13] F. Barrero, M. R. Arahal, R. Gregor, S. Toral, and M. J. Duran, "One step modulation predictive current control method for the asymmetrical dual three-phase induction machine," *IEEE Trans. Ind. Electron.*, vol. 56, no. 6, pp. 1974–1983, Jun. 2009.

[14] L. Alberti and N. Bianchi, "Impact of winding arrangement in dual 3-phase induction motor for fault tolerant applications," in *Proc. 19th Int. Conf. Electr. Mach.*, Rome, Italy, 2010, pp. 1–6.

[15] L. Alberti and N. Bianchi, "Experimental tests of dual three-phase induction motor under faulty operation condition," *IEEE Trans. Ind. Electron.*, vol. 59, no. 5, pp. 2041–2048, May 2012.

[16] M. Barcaro, N. Bianchi, and F. Magnussen, "Analysis and tests of a dual three-phase 12-slot 10-pole permanent-magnet motor," *IEEE Trans. Ind. Appl.*, vol. 46, no. 6, pp. 2355–2362, Nov./Dec. 2010.

[17] L. X. Tang and G. J. Su, "High-performance control of two three-phase permanent-magnet synchronous machines in an integrated drive for automotive applications," *IEEE Trans. Power Electron.*, vol. 23, no. 6, pp. 3047–3055, Nov. 2008.

[18] Y. S. Hu, Z. Q. Zhu, and K. Liu, "Current control for dual three-phase permanent magnet synchronous motors accounting for current unbalance and harmonics," *IEEE J. Emerg. Sel. Topics Power Electron.*, vol. 2, no. 2, pp. 272–284, Jun. 2014.

[19] M. Barcaro, A. Faggion, N. Bianchi, and S. Bolognani, "Sensorless rotor position detection capability of a dual three-phase fractional-slot IPM machine," *IEEE Trans. Ind. Appl.*, vol. 48, no. 6, pp. 2068–2078, Nov./Dec. 2012.

[20] C. M. Stephens, "Fault detection and management system for fault-tolerant switched reluctance motor drives," *IEEE Trans. Ind. Appl.*, vol. 27, no. 6, pp. 1098–1102, Nov./Dec. 1991.

[21] L. Belfore and A. Arkadan, "A methodology for characterizing fault tolerant switched reluctance motors using neurogenetically derived models," *IEEE Trans. Energy Convers.*, vol. 17, no. 3, pp. 380–384, Sep. 2002.

[22] S. Mir, M. S. Islam, T. Sebastian, and I. Husain, "Fault-tolerant switched reluctance motor drive using adaptive fuzzy logic controller," *IEEE Trans. Power Electron.*, vol. 19, no. 2, pp. 289–295, Mar. 2004.

[23] B. Lequesne, S. Gopalakrishnan, and A. M. Omekanda, "Winding short circuits in the switched reluctance drive," *IEEE Trans. Ind. Appl.*, vol. 41, no. 5, pp. 1178–1184, Sep./Oct. 2005.

[24] S. Gopalakrishnan, A. M. Omekanda, and B. Lequesne, "Classification and remediation of electrical faults in the switched reluctance drive," *IEEE Trans. Ind. Appl.*, vol. 42, no. 2, pp. 479–486, Mar./Apr. 2006.

[25] M. D. Hennen, M. Niessen, C. Heyers, H. J. Brauer, and R. W. D. Doncker, "Development and control of an integrated and distributed inverter for a fault tolerant five-phase switched reluctance traction drive," *IEEE Trans. Power Electron.*, vol. 27, no. 2, pp. 547–554, Feb. 2012.

[26] H. Torkaman and E. Afjei, "Comprehensive detection of eccentricity fault in switched reluctance machines using high-frequency pulse injection," *IEEE Trans. Power Electron.*, vol. 28, no. 3, pp. 1382–1391, Mar. 2013.

[27] W. Ding and D. L. Liang, "A fast nonlinear variable structure equivalent magnetic circuit modeling for dual-channel switched reluctance machine," *Energy Convers. Manage.*, vol. 52, no. 1, pp. 3652–3663, Sep. 2011.

[28] A. V. Radun, C. A. Ferreira and E. Richter, "Two-channel switched reluc-tance starter/generator results," *IEEE Trans. Ind. Appl.*, vol. 34, no. 5, pp. 1026–1034, Sep./Oct. 1998.

[29] W. Ding and D. L. Liang, "Dynamic modeling and performance prediction for dual channel switched reluctance machine considering mutual coupling," *IEEE Trans. Magn.*, vol. 46, no. 9, pp. 3652–3663, Sep. 2010.

[30] W. Ding, "Comparative study on dual-channel switched reluctance generator performances under single- and dual-channel operation modes," *IEEE Trans. Energy Convers.*, vol. 27, no. 3, pp. 680–688, May 2012.

[31] W. Ding, J. Y. Lou, and L. Liu, "Improved decoupled model of mutually coupled dual-channel SRM with consideration of magnetic saturation in dual-channel operation," *IET Electr. Power Appl.*, vol. 7, no. 3, pp. 427–440, Aug. 2013.

[32] W. Ding, L. Liu, J. Y. Lou, and Y. P. Liu, "Comparative studies on mutually coupled dual-channel switched reluctance machine with different winding connections," *IEEE Trans. Magn.*, vol. 49, no. 11, pp. 5574–5589, Nov. 2013.

**Wen Ding** (M'11) was born in Changde, China. He received the B.S. degree from the Xi'an University of Technology, Xi'an, China, in 2003, and the M.S. and Ph.D. degrees from Xi'an Jiaotong University, Xi'an, in 2006 and 2009, respectively, all in electrical engineering.

Since then, he has been with the Department of Electrical Machinery and the State Key Laboratory of Electrical Insulation and Power Equipment, School of Electrical Engineering, Xi'an Jiaotong University, where he is currently an Associate Professor. His research interests include switched reluctance machines, electrical drives, and power electronics.

**Yanfang Hu** was born in Shangqiu, China. She received the B.S. degree from the Shenyang University of Chemical Technology, Shenyang, China, in 2011.

In 2011, she joined the Hangzhou Hangfa Power Equipment Co., Ltd., Hangzhou, China, where she was involved in research and development of induction and synchronous motors and turbine generator for small- and medium-sized power equipment. She is currently involved in a switched reluctance motor project as a graduate student at the School of Electrical Engineering, Xi'an Jiaotong University, Xi'an, China.

**Luming Wu** was born in Ganzhou, China. He received the B.S. degree from Xi'an Jiaotong University, Xi'an, China, in 2010.

In 2010, he joined the CPI Jiangxi Nuclear Power Co. Ltd., Jiujiang, China, where he was involved in research and development of large nuclear power plant. He is currently involved in a switched reluctance motor project as a graduate student at the School of Electrical Engineering, Xi'an Jiaotong University, Xi'an, China.